The Astrophysical Journal, 974:246 (13pp), 2024 October 20 https://doi.org/10.3847/1538-4357/ad738e

Precise Measurements of TeV Halos around Geminga and Monogem Pulsars with HAWC

A. Albert[1], R. Alfaro[2], C. Alvarez[3], J. C. Arteaga-Velázquez[4], D. Avila Rojas[2], H. A. Ayala Solares[5], R. Babu[6], E. Belmont-Moreno[2], A. Bernal[2], K. S. Caballero-Mora[3], T. Capistrán[2], A. Carramiñana[7], S. Casanova[8], U. Cotti[4], J. Cotzomi[9], S. Coutiño de León[10], E. de la Fuente[11,12], D. Depaoli[13], N. Di Lalla[14], R. Diaz Hernandez[7], B. L. Dingus[1], M. A. DuVernois[10], M. Durocher[1], J. C. Díaz-Vélez[10], K. Engel[15], C. Espinoza[2], K. L. Fan[15], K. Fang[10], N. Fraija[2], J. A. García-González[16], F. Garfias[2], H. Goksu[13], M. M. González[2], J. A. Goodman[15], S. Groetsch[6], J. P. Harding[1], S. Hernández-Cadena[2], I. Herzog[6], P. Hüntemeyer[6], D. Huang[15], F. Hueyotl-Zahuantitla[3], A. Iriarte[2], V. Joshi[17], S. Kaufmann[18], D. Kieda[19], A. Lara[20], W. H. Lee[2], J. Lee[21], H. León Vargas[2], J. T. Linnemann[6], A. L. Longinotti[2], G. Luis-Raya[18], K. Malone[1], O. Martinez[9], J. Martínez-Castro[22], J. A. Matthews[23], P. Miranda-Romagnoli[24], J. A. Montes[2], J. A. Morales-Soto[4], E. Moreno[9], M. Mostafá[25], A. Nayerhoda[8], L. Nellen[26], R. Noriega-Papaqui[24], L. Olivera-Nieto[13], N. Omodei[14], Y. Pérez Araujo[2], E. G. Pérez-Pérez[18], C. D. Rho[27], D. Rosa-González[7], H. Salazar[9], D. Salazar-Gallegos[6], A. Sandoval[2], M. Schneider[15], G. Schwefer[13], J. Serna-Franco[2], Y. Son[21], R. W. Springer[19], O. Tibolla[18], K. Tollefson[6], I. Torres[7], R. Torres-Escobedo[28], R. Turner[6], F. Urea-Mena[7], E. Varela[9], L. Villaseñor[9], X. Wang[6], I. J. Watson[21], E. Willox[15], H. Wu[10], S. Yun-Cárcamo[15], H. Zhou[28], C. de León[4], and
(for the HAWC Collaboration)
M. Di Mauro[29]

[1] Los Alamos National Laboratory, Los Alamos, NM, USA
[2] Instituto de Astronomía, Universidad Nacional Autónoma de México, Ciudad de México, Mexico
[3] Universidad Autónoma de Chiapas, Tuxtla Gutiérrez, Chiapas, Mexico
[4] Universidad Michoacana de San Nicolás de Hidalgo, Morelia, Mexico
[5] Department of Physics, Pennsylvania State University, University Park, PA, USA
[6] Department of Physics and Astronomy, Michigan State University, East Lansing, MI, USA
[7] Instituto Nacional de Astrofísica, Óptica y Electrónica, Puebla, Mexico
[8] Institute of Nuclear Physics Polish Academy of Sciences, PL-31342 IFJ-PAN, Krakow, Poland
[9] Facultad de Ciencias Físico Matemáticas, Benemérita Universidad Autónoma de Puebla, Puebla, Mexico
[10] Department of Physics, University of Wisconsin-Madison, Madison, WI, USA
[11] Departamento de Física, Centro Universitario de Ciencias Exactas e Ingenierias, Universidad de Guadalajara, Guadalajara, Mexico; eduardo.delafuentea@academicos.udg.mx
[12] Doctorado en Ciencias Físic-Matematicas, Centro Universitario de los Valles, Universidad de Guadalajara, Ameca, Jalisco, Mexico
[13] Max-Planck Institute for Nuclear Physics, 69117 Heidelberg, Germany
[14] Department of Physics, Stanford University: Stanford, CA 943054060, USA
[15] Department of Physics, University of Maryland, College Park, MD, USA
[16] Tecnologico de Monterrey, Escuela de Ingeniería y Ciencias, Ave. Eugenio Garza Sada 2501, Monterrey, N.L. 64849, Mexico
[17] Erlangen Centre for Astroparticle Physics, Friedrich-Alexander-Universität Erlangen-Nürnberg, Erlangen, Germany
[18] Universidad Politecnica de Pachuca, Pachuca, Hgo, Mexico
[19] Department of Physics and Astronomy, University of Utah, Salt Lake City, UT, USA
[20] Instituto de Geofísica, Universidad Nacional Autónoma de México, Ciudad de México, Mexico
[21] University of Seoul, Seoul, Republic of Korea
[22] Centro de Investigación en Computación, Instituto Politécnico Nacional, México City, Mexico
[23] Dept of Physics and Astronomy, University of New Mexico, Albuquerque, NM, USA
[24] Universidad Autónoma del Estado de Hidalgo, Pachuca, Mexico
[25] Department of Physics, Temple University, Philadelphia, PA, USA
[26] Instituto de Ciencias Nucleares, Universidad Nacional Autónoma de México, Ciudad de México, Mexico
[27] Department of Physics, Sungkyunkwan University, Suwon 16419, Republic of Korea
[28] Tsung Dao Lee Institute, Department of Physics & Astronomy, Shanghai Jiao Tong University, Shanghai, People's Republic of China; torresramiro350@sjtu.edu.cn, hao_zhou@sjtu.edu.cn
[29] Istituto Nazionale di Fisica Nucleare, Sezione di Torino: Turin, Italy; dimauro.mattia@gmail.com
Received 2024 February 3; revised 2024 August 4; accepted 2024 August 5; published 2024 October 16

Abstract

We present the most precise measurements to date for the spatial extension and energy spectrum of the γ-ray region between a pulsar's wind nebula and the interstellar medium, better known as the halo, present around Geminga and PSR B0656+14 (Monogem) using ∼2398 days of >1 TeV data collected by the HAWC observatory. We interpret the data using a physically motivated model for the diffuse γ-ray emission generated from positrons and electrons ($e^{\pm}$) injected by the pulsar wind nebula and inverse Compton scattering with interstellar radiation fields. We find the morphologies of the regions inside these halos are characterized by an inhibited diffusion that are approximately three orders of magnitudes smaller than the Galactic average. We also obtain the $e^{\pm}$ emission efficiencies of 6.6% and 5.1%, respectively, for Geminga and Monogem. These results have remarkable consequences for the study of the particle diffusion in the region between the pulsar wind nebulae and the interstellar medium, and for the interpretation of the flux of positrons measured by the AMS-02 experiment above 10 GeV.

Unified Astronomy Thesaurus concepts: High energy astrophysics (739); Particle astrophysics (96); Pulsars (1306); Pulsar wind nebulae (2215)

1. Introduction

The first detection of TeV emission around the pulsar Geminga (PSR J0633+1746) was reported by Milagro with an angular size of $2^\circ\!.8 \pm 0.^\circ 8$ (A. A. Abdo et al. 2007). The HAWC collaboration confirmed this observation and reported the detection of an extended gamma-ray (γ-ray) halo around Geminga with an extension of $5.^\circ 5 \pm 0.^\circ 7$ and around Monogem (PSR B0656+14) with an extension of $4.^\circ 8 \pm 0.^\circ 6$ (A. U. Abeysekara et al. 2017a, hereafter referred to as HAWC2017), respectively. The HAWC collaboration further reported a number of extended halos around other Galactic pulsars in the 3HWC source catalog (A. Albert et al. 2020). The most recent detection of a halo is located around PSR J0359+5414 (A. Albert et al. 2023). γ-ray halos around pulsars are generated from electrons and positrons accelerated by pulsar wind nebulae (PWNe) and inverse Compton scattering (ICS) on the low-energy photon fields present in the Galaxy. These emissions have become a new subclass of galactic γ-ray sources referred to as "pulsar halos," "TeV halos," or "inverse Compton halos" (M. Di Mauro et al. 2020; D. Hooper & T. Linden 2022). We will use in this paper the former name, which is more generic than the other two. In fact, extended halos around pulsars can be measured also at GeV energies, and they could be generated in major part by ICS with a contribution from synchrotron radiation. Criteria to identify TeV halos and the number of possible candidates are discussed in T. Sudoh et al. (2019), G. Giacinti et al. (2020), M. Di Mauro et al. (2020), and R. Lopez-Coto et al. (2022). Since pulsar halos are generated by ICS of $e^{\pm}$ injected by PWNe, pulsar halo candidates are of great interest because their detection would provide further evidence that PWNe efficiently accelerate positrons and electrons and that PWNe are likely the main contributors to the anomalous local positron excess measured by PAMELA, Fermi-LAT, and AMS-02 (D. Hooper et al. 2017; I. Cholis et al. 2018; L. Orusa et al. 2021).

High-energy cosmic rays have been measured by PAMELA (O. Adriani et al. 2013), then Fermi-LAT (M. Ackermann et al. 2012), and with unprecedented precision AMS-02 (M. Aguilar et al. 2019) measured high-energy cosmic-ray (CR) positrons (e^+). AMS-02 recently released the 7 yr data for the flux of cosmic e^+ up to 1 TeV (M. Aguilar et al. 2021), showing a prominent excess with respect to the secondary component, which is due to the spallation of CRs with atoms of the interstellar medium (e.g., I. V. Moskalenko & A. W. Strong 1998; T. Delahaye et al. 2009; M. Di Mauro et al. 2014). This excess is called positron excess, and its spectral shape suggests the presence of primary e^+ sources in our Galaxy. Since very high-energy e^+ suffer intense energy losses while propagating in the Galaxy, AMS-02 observations require this primary source to be within a few kpc from the Earth. PWNe have been considered as a primary source of high-energy $e^{\pm}$ for more than a decade (e.g., J. P. Ostriker & J. E. Gunn 1969; R. E. Lingenfelter 1973; A. K. Harding & R. Ramaty 1987; A. M. Atoyan et al. 1995; F. A. Aharonian et al. 1995; D. Hooper et al. 2009; M. Di Mauro et al. 2014; D. Hooper et al. 2017; L. Orusa et al. 2021). This makes the interpretation of the positron excess e^+ injected by PWNe one of the most physically motivated interpretations (e.g., D. Hooper et al. 2017; L. Orusa et al. 2021).

The HAWC observations of γ-ray halos around the Geminga and Monogem pulsars can thus provide important information about the acceleration of $e^{\pm}$ from PWNe and can be used to demonstrate that the nearby and more powerful pulsars, i.e., with large spin-down luminosities, are finally giving the evidence that these sources contribute to the positron excess (D. Hooper et al. 2017; M. Di Mauro et al. 2019).

The extension of the γ-ray halos around Geminga and Monogem suggests that a diffusion coefficient D 2 to 3 orders of magnitude smaller than the average in the Galaxy is needed. In fact, the estimate for the value of D performed using HAWC data for Geminga and Monogem gives a value of $D \sim 4.5 \times 10^{27}\,\mathrm{cm^2\,s^{-1}}$ at 100 TeV, while the value needed to fit CR data is about $\sim 1-3 \times 10^{30}\,\mathrm{cm^2\,s^{-1}}$ at the same energy (V. S. Berezinskiĭ et al. 1990; R. Trotta et al. 2011; M. Korsmeier & A. Cuoco 2022). Suppressed diffusion around PWNe is challenging to explain theoretically (e.g., C. Evoli et al. 2018; S. Recchia et al. 2021; P. Mukhopadhyay & T. Linden 2022; B. Schroer et al. 2023).

We present in this paper an updated study of the γ-ray morphology of Geminga and Monogem using $\sim$2398 days of data from the HAWC observatory. The present work better constrains the diffusion coefficients in the region of these two pulsars. We utilize a physically motivated model of diffuse emission generated from ICS emission interactions of electrons/positrons injected with a power law with a cutoff spectral shape for diffusion coefficients between $10^{25}\,\mathrm{cm^2\,s^{-1}}$ to $10^{27}\,\mathrm{cm^2\,s^{-1}}$ at 1 GeV. Additionally, we take into account emission from a third source, 3HWC J0631-107 (A. Albert et al. 2020) that is associated with the pulsar PSR J0631.5+1036 (hereafter J0631) with an age of 43 kyr at a distance of 2.1 kpc and $\dot{E} = 1.7 \times 10^{35}\,\mathrm{erg\,s^{-1}}$ (R. N. Manchester et al. 2005).

The paper is divided into the following sections. The model of extended γ-ray emission from inverse Compton interactions with the light from interstellar radiation fields (ISRFs) is discussed in Section 1. The HAWC detector and data selection are discussed in Section 2. In Section 3, we describe the analysis framework. The results from this multisource analysis are presented in Section 4. Sections 5 and 6 summarize the results and highlight their importance based on our current understanding of TeV halos with Geminga-like characteristics.

2. Gamma-Ray Model

In this section, we describe the physical model employed for generating the templates we fit to the data.

We are interested in the extended γ-ray halo at TeV energies and a few degrees around PWNe. These γ-rays are produced by $e^{\pm}$ pairs accelerated and escaped from the PWN and ICS against the ISRF's low-energy photons. The Galactic ISRF is composed of the cosmic microwave background (CMB), described by a blackbody energy density at temperature $T_{\rm CMB} = 2.753$ K, the IR light with the peak of the spectrum at $T_{\rm IR} = 3.5 \times 10^{-3}$ eV, and by the stellar light (SL) with $T_{\rm SL} = 0.3$ eV (S. Vernetto & P. Lipari 2016; C. C. Popescu et al. 2017). The study of small-scale regions in the range of a few arcseconds to arcminutes observed in the nebula, typically measured in X-ray energies (e.g., B. Posselt et al. 2017, for Geminga), is beyond the scope of this paper and the angular resolution of HAWC (A. Albert et al. 2024). The model has been extensively used in previous papers (M. Di Mauro et al. 2019, 2020, 2021). The model assumes that electrons and positrons are injected in the interstellar medium by the PWN following the spin-down power of the pulsar. Once the $e^{\pm}$ travel in the interstellar space, they encounter different processes due to CR propagation—in particular, diffusion of the Galactic magnetic field inhomogeneities and energy losses due to inverse Compton scattering and synchrotron radiation. Other process and energy losses are subdominant for electrons and positrons with energies below 10 GeV.

The photon flux emitted for the ICS by a source, in a solid angle $\Delta\Omega$ and at an energy E_γ, is written as

$$\phi^{\rm IC,\,Sync}(E_\gamma, \Delta\Omega) = \frac{1}{4\pi}\int_{\max(E_\gamma, m_e c^2)}^{\infty} dE\,\mathcal{M}(E, \Delta\Omega)\mathcal{P}^{\rm IC}(E, E_\gamma). \quad (1)$$

The term $\mathcal{P}^{\rm IC}(E, E_\gamma)$ denotes the power of photons emitted by $e^{\pm}$ from ICS emissions. Furthermore, $\mathcal{M}(E, \Delta\Omega)$ represents the spectrum of e^{+} and e^{-} of energy E propagating in the Galaxy, and it is calculated as follows:

$$\mathcal{M}(E, \Delta\Omega) = \int_{\Delta\Omega} d\Omega \int_0^{\infty} ds\,\mathcal{N}_e(E, s). \quad (2)$$

$\mathcal{N}_e(E, s)$ is the energy spectrum of $e^{\pm}$ of energy E emitted by the source, and s is the distance along the line of sight.

The ICS power of a photon of energy E_γ produced by an electron of energy E is calculated as

$$\mathcal{P}^{\rm IC}(E, E_\gamma) = \frac{3\sigma_T c\, m_e^2 c^4}{4E^2}\int_{\frac{m_e c^2}{4E}}^{1} dq \frac{d\mathcal{N}}{d\epsilon}(\epsilon(q)) \times\left(1 - \frac{m_e^2 c^4}{4qE^2(1-\tilde{\epsilon})}\right) \times\left[2q\log q + q + 1 - 2q^2 + \frac{\tilde{\epsilon}(1-q)}{2-2\tilde{\epsilon}}\right], \quad (3)$$

where ϵ is the ISRF photon energy, $\frac{d\mathcal{N}}{d\epsilon}(\epsilon(q))$ is the energy spectrum of the ISRF, and

$$q = \frac{\tilde{\epsilon}}{\Gamma_\epsilon(1-\tilde{\epsilon})},\quad \Gamma_\epsilon = \frac{4\epsilon E}{m_e^2 c^4},\quad \tilde{\epsilon} = \frac{E_\gamma}{E}. \quad (4)$$

We assume that the ISRF is homogeneous, and we use the spectrum found in the local Galaxy in (S. Vernetto & P. Lipari 2016). Our results do not change when using the model for the local Galaxy in C. C. Popescu et al. (2017).

The model assumes continuous $e^{\pm}$ emission from the PWNe with a rate proportional to the pulsar spin-down energy. Under the continuous injection, the injection spectrum ($Q(E, t)$) is energy- and time-dependent and can be expressed as

$$Q(E, t) = L(t)\left(\frac{E}{E_0}\right)^{-\gamma}\exp\left(-\frac{E}{E_c}\right), \quad (5)$$

where the $L(t)$ incorporates time dependence of the $e^{\pm}$ emission, and E_c is a cutoff energy for which values above tens of TeV energies are necessary to produce γ rays through ICS at the energies measured around the Geminga PWN with HAWC and Milagro. $L(t)$ varies due to magnetic dipole braking according to

$$L(t) = \frac{L_0}{\left(1 + \frac{t}{\tau_0}\right)^2}. \quad (6)$$

The normalization of the power law is fixed to $E_0 = 1$ GeV. The total energy emitted by a pulsar in $e^{\pm}$ is given by

$$E_{\rm tot} = \int_0^T dt \int_{E_1}^{\infty} dE E Q(E, t) = \int_0^T dt L(t). \quad (7)$$

The normalization L_0 for a single PWN is obtained by assuming that a fraction η of the total spin-down energy W_0 emitted by the pulsar is released in form of $e^{\pm}$ pairs, i.e.,

$$E_{\rm tot} = \eta W_0. \quad (8)$$

The value of W_0 is obtained from the age of the pulsar T, the typical pulsar decay time τ_0, and the spin-down luminosity $\dot{E}$:

$$W_0 = \tau_0 \dot{E}\left(1 + \frac{T}{\tau_0}\right)^2. \quad (9)$$

The spin-down luminosity $\dot{E}$, the observed age $t_{\rm obs}$ (where $T = t_{\rm obs} + d/c$ is the actual age), and the distance d for the pulsars are taken from the ATNF catalog (R. N. Manchester et al. 2005). The characteristic pulsar spin-down timescale τ_0 is assumed to be $\tau_0 = 12$ kyr, while the magnetic braking index is assumed to be $k = 3$, which was assumed in HAWC2017 from F. A. Aharonian et al. (1995). We consider $d = 250$ pc, $t_{\rm obs} = 370$ kyr, and $\dot{E} = 3.2 \times 10^{34}$ erg s^{-1} for Geminga, and $d = 288$ pc, $t_{\rm obs} = 110$ kyr, and $\dot{E} = 3.8 \times 10^{34}$ erg s^{-1} for Monogem (R. N. Manchester et al. 2005). In the continuous injection scenario and with homogeneous diffusion in the Galaxy, the flux $\mathcal{N}_e(E, \boldsymbol{r}, t)$ of $e^{\pm}$ at an energy E, a position $\boldsymbol{r}$, and time t is given by the following equation (H. Yuksel et al. 2009):

$$\mathcal{N}_e(E, \boldsymbol{r}, t) = \int_0^t dt_0 \frac{b(E_s(t_0))}{b(E)}\frac{1}{(\pi\lambda^2(t_0, t, E))^{\frac{3}{2}}} \times\exp\left(-\frac{|\boldsymbol{r} - \boldsymbol{r}_s|^2}{\lambda(t_0, t, E)^2}\right)Q(E_s(t_0)), \quad (10)$$

where the integration over t_0 is included because the PWN releases $e^{\pm}$ continuously in time. $b(E)$ is the function that includes the energy losses for ICS and synchrotron radiation, $\boldsymbol{r}_s$ indicates the source position, and λ is the typical propagation scale length:

$$\lambda^2 = \lambda^2(E, E_s) \equiv 4\int_E^{E_s} dE' \frac{D(E')}{b(E')}, \quad (11)$$

with the diffusion coefficient $D(E)$ given by $D(E) = D_0(E/1\,{\rm GeV})^{\delta}$. E_s is the initial energy of $e^{\pm}$ that cools down to E during the loss

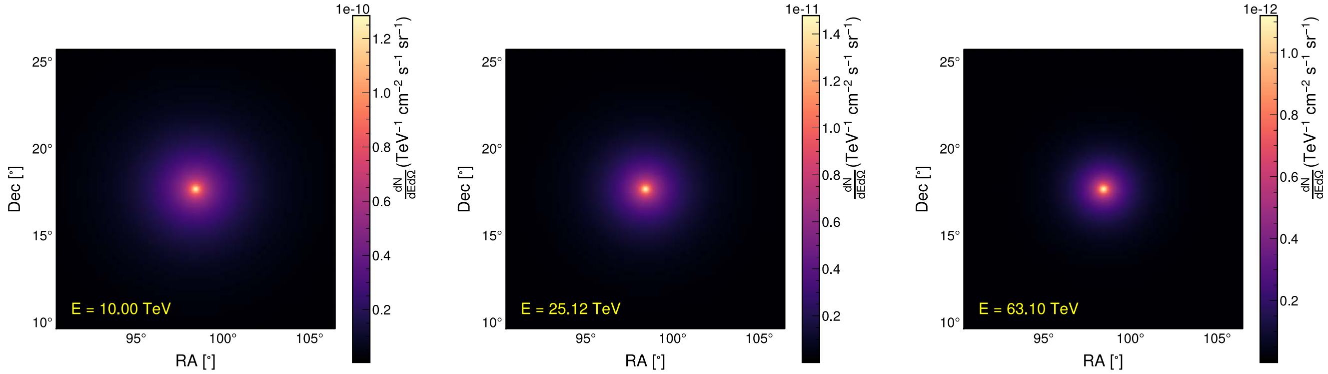

Figure 1. Example of intensity maps of the Geminga ICS γ-ray emission at energies of 10 TeV (left), 25 TeV (middle), and 63 TeV (right). The diffusion coefficient assumed is $D_0 = 1.3 \times 10^{26}$ cm^2 s^{-1} and $\alpha_e = 1.8$ for a region of $15° \times 15°$ around the pulsar.

time $\Delta\tau$:

$$\Delta\tau(E, E_s) \equiv \int_E^{E_s} \frac{dE'}{b(E')} = t - t_{\rm obs}. \quad (12)$$

We assume for δ a value of $1/3$, as previously done also in the work of A. U. Abeysekara et al. (2017a), M. Di Mauro et al. (2019), T. Sudoh et al. (2019), G. Giacinti et al. (2020), M. Di Mauro et al. (2020), and R. Lopez-Coto et al. (2022). The energy range considered in our analysis is between 1 and 300 TeV. However, the peak sensitivity is reached in the range 5–50 TeV. This variation of energy is too limited to permit a determination of δ.

3. HAWC Observatory and Data Selection

3.1. HAWC Detector

The High Altitude Water Cherenkov (HAWC) γ-ray Observatory is located in Puebla, Mexico on Sierra Negra at an elevation of 4100 m. HAWC is composed of 300 water Cherenkov detectors (WCDs). Each WCD (7.3 m in diameter and 4.5 m in height) houses 200,000 liters of ultrapurified water and is equipped with four photomultiplier tubes (PMTs; three peripheral 8″ PMTs with a central 10″ PMT). The full array has an effective detection area of 22,000 m^2. For a full description of the HAWC detector operations, see A. J. Smith (2016) and A. U. Abeysekara et al. (2019, 2023).

HAWC has an active duty cycle of >95% combined with an instantaneous field of view of 2 sr; it can observe $2/3$ of the northern sky. It is sensitive to sources with declinations of $-26°$ to $+64°$ for energies between 300 GeV up to 100 TeV (A. U. Abeysekara et al. 2023).

3.2. Data Selection

We utilize ~2398 of days of *Pass 5* data (A. Albert et al. 2024) collected between 2015 June and 2022 July from the HAWC observatory. The data are binned according to a 2D scheme of estimated energy ($\hat{E}$) with quarter-decade bin widths in $\log_{10}$ and fraction of detector active during an air-shower event. The energy bins extend from $\hat{E} = 1$ TeV to $\hat{E} = 316$ TeV using the "Neural Network" (NN) energy estimator introduced in A. U. Abeysekara et al. (2019). The NN energy estimator consists of a two hidden layer node NN map with a total of 479 weights. The primary energy of γ-ray is estimated from air-shower parameters that are measured during the standard HAWC reconstruction process.

We selected a region of interest (ROI) with a radius of 8° centered in between Geminga and Monogem. In addition to Geminga and Monogem, we see the emission of 3HWC J0631-107.

4. Analysis Approach

The model for the analysis is implemented using spatial template mapcubes that consist of skymaps that span over R.A. and decl., where each map corresponds to γ-ray intensity maps at different energy bands from electron ICS interactions as they escape the pulsar. Each template is binned in energy for the range of 0.1 TeV, with each pixel having units of (TeV^{-1} cm^{-2} s^{-1} sr^{-1}) for a region of $15° \times 15°$ around the source, Geminga and Monogem in this case (see Figure 1). The left panel shows more extended morphology because the e$^{\pm}$ cooling time is comparable to the pulsar age for $\leqslant$1 TeV. Therefore, e$^{\pm}$s can travel distances on the scale of tens of parsecs before experiencing energy losses (see Figure 3 of R.-Y. Liu 2022). However, the e$^{\pm}$ experience increasing energy losses that shows a more compact morphology as depicted in the middle and right panels of Figure 1. The mapcubes are stored in FITS files that follow the same format used in Fermi-LAT and the fluxes estimates are from M. Di Mauro et al. (2019).

We use a grid of template mapcubes for diffusion coefficients in the range 10^{25}–10^{27} cm^2 s^{-1} at 1 GeV electron energy, with electron spectral index values of $\alpha_e = 0.0$–2.2.

A custom spatial model was developed for the analysis of HAWC data with the aforementioned templates, which allows for the interpolation of template map parameters, i.e., diffusion coefficient and injection spectral index in this case. This generates a look-up table that is used during parameter sampling. A similar process is used for the spectral shape, which uses spectral flux estimates from M. Di Mauro et al. (2019) with a power-law spectral shape with an exponential cutoff at 100 TeV. These flux values are integrated over a region of 30° around the pulsar to maximize the containment of the extended γ-ray emission for energies between 1 and 10 TeV.

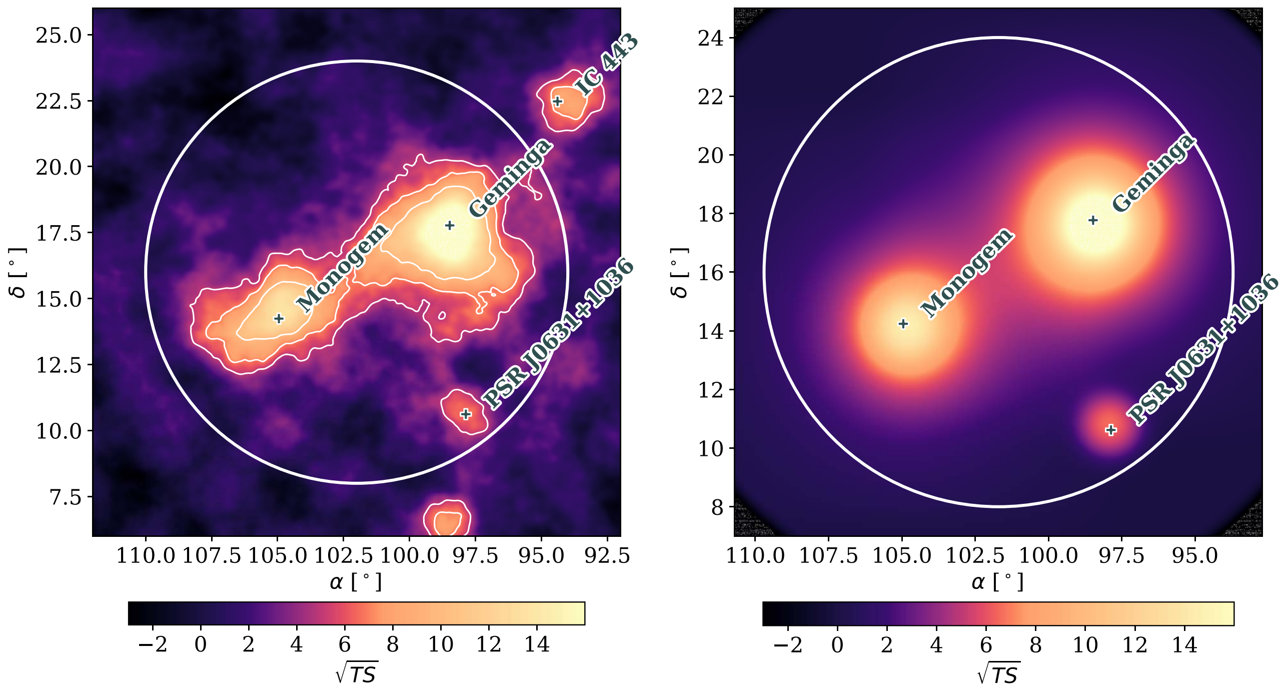

Figure 2. Left: HAWC significance map region, for reconstructed energies between 1 TeV and 316 TeV. Right: Model map assuming best-fit parameters in analysis. The map is in equatorial coordinates. The significance is calculated by assuming a 1° disk for each pixel with a power-law spectral shape of $\alpha_\gamma = -2.25$. The contours show the 5σ, 7σ, and 10σ levels. Source outside the ROI is the supernova remnant IC 443. The white circle illustrates the ROI in both figures.

Table 1
Best-fit Results

Source	R.A. ± stat (°)	Decl. ± stat (°)	η ± stat ± syst [10^{-2}]	α_e ± stat ± syst	D_0 ± stat ± syst [10^{26} cm^2 s^{-1}]	TS
Geminga	98.69 ± 0.02	17.57 ± 0.02	$6.60 \pm 0.7 \pm 2.5$	$0.95^{+0.08}_{-0.09} \pm 0.32$	$1.07^{+0.21}_{-0.18}\,^{+0.73}_{-0.43}$	1010
Monogem	105.06 ± 0.02	14.34 ± 0.02	$5.10^{+0.80}_{-0.70} \pm 2.7$	$1.06^{+0.09}_{-0.10} \pm 0.14$	$1.47^{+0.14}_{-0.24}\,^{+1.5}_{-0.73}$	481
Geminga*	…	…	$8.70 \pm 0.40 \pm 4.10$	$1.30 \pm 0.50 \pm 0.40$	$1.05 \pm 0.11\,^{+1.20}_{-0.66}$	982
Monogem*	…	…	$1.90 \pm 0.49 \pm 0.49$	$0.72 \pm 0.14 \pm 0.53$	$1.05 \pm 0.11\,^{+1.20}_{-0.66}$	400

Notes. The columns list the best-fit position, emission efficiency η, injection spectral index α_e, diffusion D_0 coefficient at an electron energy of 1 GeV, and the test statistic. The * indicates the best-fit values for the joint fit of diffusion coefficient.

For J0631, we have assumed a simple power-law spectral shape:

$$\Phi(E_\gamma) = \phi_0 \left(\frac{E_\gamma}{E_0}\right)^{-\alpha}. \tag{13}$$

The pivot (E_0) is chosen at 20 TeV with flux normalization (ϕ_0) and spectral index α_γ set free during the likelihood fit. For the spatial shape, we have used a symmetric Gaussian model described by

$$\frac{dN}{d\Omega} = \left(\frac{180}{\pi}\right)^2 \frac{1}{2\pi\sigma^2} \exp\left(-\frac{\theta^2}{\sigma^2}\right), \tag{14}$$

where θ is the angular distance, and σ is the Gaussian width used to measure the size of the extended source. The parameter σ is fit to the data.

The parameters of interest are $e^\pm$ emission efficiency, η, diffusion coefficient D_0, electron spectral index α_e. We evaluated the best-fit parameter values using a multisource likelihood fit with the multi-mission maximum likelihood (3ML)[30] Python framework (G. Vianello et al. 2015), which handles data from different observatories via a common plugin scheme. The specific plugin for the HAWC observatory is the HAWC Accelerated Likelihood plugin (HAL)[31] (A. U. Abeysekara et al. 2021). Moreover, the custom spatial shape and spectral shape are part of the astromodels,[32] an astrophysical model package interface with 3ML.

5. Results

5.1. Best-fit Results

Figure 2 shows the significance map (left panel) of the Geminga region with the pass 5 NN map and the model map (right panel) assuming the best-fit values listed in Table 1. We see a maximum significance of 20.9σ for Geminga, 14.7σ for Monogem, and 6.4σ for J0631. Figure 3 shows the residual map (significance map after source subtraction, assuming

[30] https://github.com/threeML/threeML
[31] https://github.com/threeML/hawc_hal
[32] https://github.com/threeML/astromodels

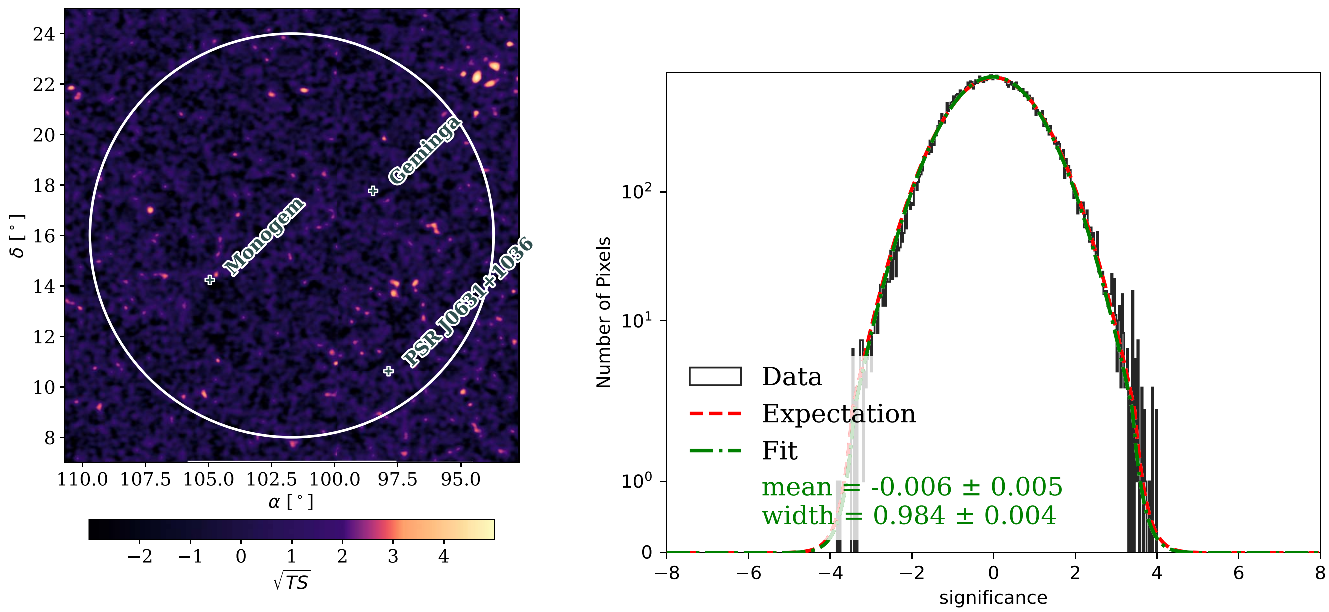

Figure 3. Left panel: significance map after subtraction of the best-fit model from HAWC data. The significance map is calculated assuming a point-source morphology to prevent any pixel correlation, which occurs for an extended source assumption. The white circle represents the ROI shown in Figure 2. Right panel: significance histogram of residuals within the ROI.

Table 2
Best-fit Results for J0631

Source	R.A. ± stat (°)	Decl. ± stat (°)	ϕ_0 ± stat [10^{-16} TeV^{-1} cm^{-2} s^{-1}]	α_γ± stat	$\sigma_{\rm ext}$ ± stat (°)	TS
PSR J0631+1036	97.87 ± 0.026	10.72 ± 0.02	$7.60^{+2.10}_{-1.90}$	$-2.25^{+0.12}_{-0.11}$	$0.380^{+0.10}_{-0.09}$	50

Note. The extension is the Gaussian width.

best-fit results). The right panel shows a one-dimensional significance histogram for the region within the ROI.

For each of the sources, we calculate a test statistic (TS), which is defined as twice the likelihood ratio test,

$$\mathrm{TS} = 2\ln\left(\frac{\mathcal{L}_s}{\mathcal{L}_N}\right), \tag{15}$$

where $\mathcal{L}_s$ is the best-fit hypothesis that contains the best-fit model with all the sources we have identified within the ROI and $\mathcal{L}_N$ is the null hypothesis (S. S. Wilks 1938). Within the scope of Wilks' theorem, the significance, $\sqrt{\mathrm{TS}}$, can be approximated by the standard deviation of a Gaussian distribution. The validity of Wilks' theorem for HAWC data is discussed in A. U. Abeysekara et al. (2017b).

The best-fit results for Geminga suggest an efficiency $\eta = 6.6 \pm 0.7\%$, $\alpha_e = 0.95^{+0.08}_{-0.09}$, and $D_0 = 1.07^{+0.21}_{-0.8} \times 10^{26}\ \mathrm{cm^2\,s^{-1}}$; those for Monogem are $\eta = 5.1^{+0.8}_{-0.7}\%$, $\alpha_e = 1.06^{+0.09}_{-0.10}$, and $D_0 = 1.47^{+0.14}_{-0.24} \times 10^{26}\ \mathrm{cm^2\,s^{-1}}$. The best-fit results suggest a TS = 1010 for Geminga and a TS = 481 for Monogem. This corresponds to a significance $\sqrt{\mathrm{TS}}$ of 31σ and 21σ, respectively. We further performed a joint fit of the diffusion coefficient for Geminga and Monogem and derived a diffusion coefficient of $D_0 = (1.05 \pm 0.11) \times 10^{26}\ \mathrm{cm^2\,s^{-1}}$ with TS values of 982 and 400 for Geminga and Monogem, respectively. We list the best-fit parameters for J0631 in Table 2 because of differences in the models. The best extension is $(0.38^{+0.10}_{-0.09})°$, $\phi = 7.16^{+2.1}_{-1.9} \times 10^{-16}\ (\mathrm{TeV^{-1}\,cm^{-2}\,s^{-1}})$, $\alpha_\gamma = 2.25^{+0.12}_{-0.11}$, with a TS of 50 that corresponds to a $\sqrt{\mathrm{TS}}$ of 7.07σ. We find that the emission from J0631 does not affect the diffusion coefficients for Geminga and Monogem.

We thus find parameters for the injection of electrons and positrons from Geminga and Monogem that are quite similar. In particular, the best-fit values for the spectral index are quite hard, ∼1.1, and the necessary efficiency is between 4% and 6%. Moreover, a similar diffusion coefficient of the order of $D_0 = 1 - 1.5 \times 10^{26}\ \mathrm{cm^2\,s^{-1}}$ is required for both sources to explain the extension of the γ-ray halos. Therefore, we confirm that a diffusion coefficient inhibited by about three orders of magnitude with respect to the Galactic average is needed. Similar results have been found by A. U. Abeysekara et al. (2017b) and M. Di Mauro et al. (2019).

5.2. Energy Range

We follow the procedure from A. U. Abeysekara et al. (2017c) to determine the energy values for which the TS varies by $\Delta\mathrm{TS} \pm 1$. The spectral shape is fixed to the best-fit values from Table 1 and multiplied with a step function with an artificial cutoff. This process is applied for the lower and upper limits. We determine the detection energy range with limits

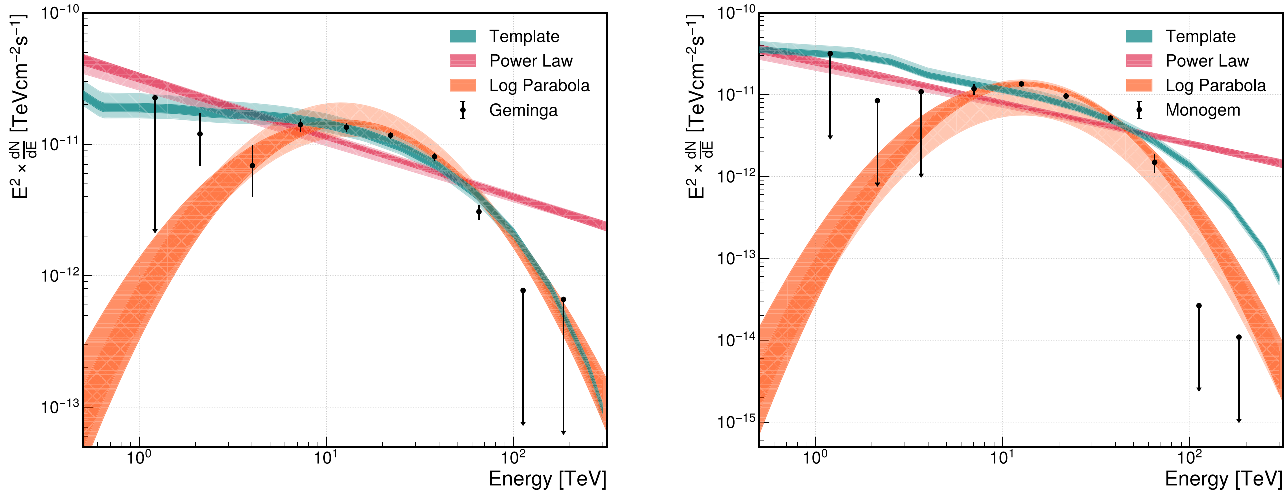

Figure 4. Spectral fit of Geminga (left) and Monogem (right). The darker bands show the statistical uncertainties, while the lighter band shows the systematic uncertainties. The fits for power-law and log parabola are shown for the same diffusion coefficient obtained from best-fit results. For energies where source is not significantly detected, we show a 90% confidence level upper limit.

defined as $E_{\min} + 1\sigma$ to $E_{\max} - 1\sigma$. We find an energy range of 1.8–75 TeV for Geminga and 5.4–68 TeV for Monogem.

5.3. Spectra

The SED for Geminga and Monogem are shown in Figure 4 for the energy ranges discussed in Section 5.2.

We remind the reader that the spatial templates shown in Figure 1 are normalized with fluxes that are integrated for a field of view of 30°. This is to ensure we take into account the excess emission for GeV energies that are below the energy range of HAWC. Because of the increasing energy losses, the size of gamma-ray emission only decreases for energies >1 TeV, which is appropriate for the HAWC energy range.

The teal band in Figure 4 shows the best fit, the $\pm 1\sigma$ statistical uncertainties are shown by the darker band, and the systematic uncertainty is shown by the lighter band. In both cases, the SED shows a break above the maximum energy of the source in a burst-like injection scenario. The maximum energy is estimated by $1/bt_{\rm age}$ where b is the energy-loss rate, and $t_{\rm age}$ is the age. For typical energy loses of 5×10^{-17} GeV^{-1} s^{-1} and using the age of Geminga, this result is $\sim$1 TeV and and $\sim$2 TeV for Monogem. This feature can be observed in both e^+ and γ-ray spectra (see for example, Figure 2 of G. Johannesson et al. 2019). Above this break, the γ-ray spectrum is dominated by continuous injection. At multi-TeV energies, we observe that the spectrum softens because of the increasing $e^{\pm}$ energy losses.

In Figure 4, we show the comparison of three spectral shapes for Geminga and Monogem with the same data used in Table 1. During the comparison, we kept the parameters of J0631 fixed to reduce the number of free parameters during the fit. The crimson band shows the fit assuming a power law, and the orange band shows the fit with a log parabola. In the case of power-law spectral shape and log parabola, we assume the spatial model introduced in HAWC2017. The diffusion coefficient is fixed for all spectral templates here to the diffusion coefficients listed in Table 1. The goodness of fit is listed in Table 3.

We use the ΔTS for the comparison of nested models and the Bayesian information criterion (BIC) and Akaike (AIC) information criterion for the comparison of non-nested models

Table 3
Comparison of Three Spectral Morphologies for Geminga and Monogem

Model	$-\log(\mathcal{L})$	AIC	BIC
Power	513952	1026992	1027074
Log	513287	1026588	1026684
Template	513328	1026675	1026799

Note. The values for log-likelihood, AIC, and BIC are the summed values for both sources.

to distinguish the preferred spectral morphology for Geminga and Monogem. Both BIC and AIC provide a way to estimate the model quality that prevents overfitting, with a penalty for models with higher number of parameters in a model (R. E. Kass & A. E. Raftery 1995; A. R. Liddle 2007). In all cases, we fix the parameters of J0631 to the best-fit values from Table 2. The power-law spectral shape has the highest AIC and BIC values and is therefore disfavored. The power-law and log parabola multisource models have a ΔTS of 1330; the log parabola is the preferred spectral shape. Since the template and log parabola spectral shape are not nested models, we use the AIC and BIC statistic criteria to compare the two models. The differences are ΔBIC = 115 and ΔAIC = 87. These values are included in Table 3. Although the log parabola has a lower BIC and AIC values compared to the other two models, it is not a physically motivated spectral shape. We therefore favor the template model, as it is directly derived from the pulsar properties.

The best-fit values for the power law (crimson band) and log parabola (orange band) for Geminga and Monogem are listed in Table 4.

We see no γ-ray emission for Geminga or Monogem beyond 100 TeV. The statistical uncertainty is obtained from the best-fit results. We estimate the systematic uncertainties by repeating the multisource fit with a set of different response functions that arise from the detector performance and simulations, as outlined in A. U. Abeysekara et al. (2019).

The spectral index reported on Table 1 suggests a harder index compared to HAWC2017 for Geminga and Monogem

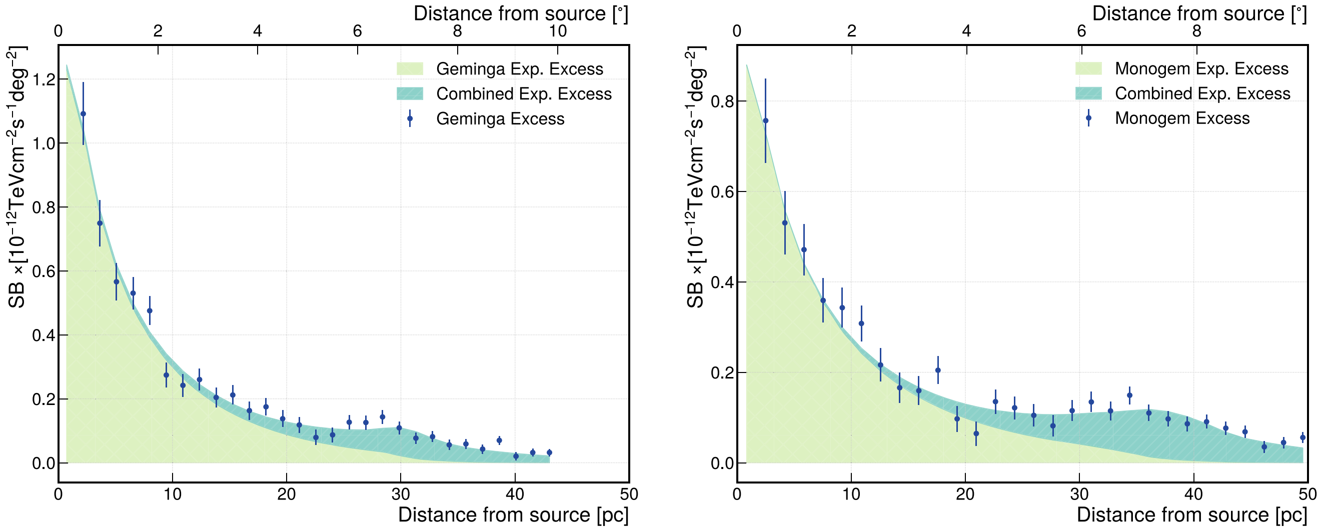

Figure 5. Surface brightness profiles of multi-TeV γ-ray emission in units of TeV cm^{-2} s^{-1} deg^{-2} as a function of distance for Geminga (left panel) and Monogem (right panel) for energy range of 5.4 to 68 TeV. The green color band shows the individual emission and the blue band shows the excess emission from its neighboring source.

Table 4
Best-fit Parameters for Monogem and Geminga Assuming the Power-law (Crimson Band; Left Section of Table) and Log Parabola Spectral (Orange Band; Right Section of Table) Shapes Shown in Figure 4 (Right Panel)

Parameter	Monogem			Geminga		
	Best-fit Value	Statistical Uncertainty	Systematic Uncertainty	Best-fit Value	Statistical Uncertainty	Systematic Uncertainty
ϕ_0 [10^{-14} (TeV cm^2 s)$^{-1}$]	1.10	$^{+0.06}_{-0.05}$	$\pm$0.21	1.50	$^{+0.06}_{-0.05}$	$\pm$0.21
α	$-$2.48	$\pm$0.03	$\pm$0.11	$-$2.47	$^{+0.02}_{-0.09}$	$\pm$0.10
ϕ_0 [10^{-14} (TeV cm^2 s)$^{-1}$]	2.20	$^{+0.12}_{-0.11}$	$\pm$13.6	2.45	$^{+0.12}_{-0.11}$	$\pm$0.43
α	$-$2.69	$\pm$0.08	$\pm$1.5	$-$2.43	$\pm$0.06	$\pm$0.22
β	0.79	$\pm$0.10	$\pm$0.87	0.50	$\pm$0.07	$\pm$0.26

because of the assumed spectral shape. However, as shown in Figure 4 the flux points follow the overall fit within $\pm 1\sigma$.

5.4 Surface Brightness

Figure 5 shows the surface brightness (SB) profile of multi-TeV γ-ray emission assuming the best-fit results in Table 1. The SB profiles are shown as a function of distance from the sources, Geminga (left panel) and Monogem (right panel), expressed in units of TeV cm^{-2} s^{-1} deg^{-2}. We show the SB profiles for the common energy range of 5.4 to 68 TeV (obtained from Section 5.2) for consistency between the two sources. Moreover, we subtract the emission from J0631 from data when calculating the SB profiles. The data show the excess emission, with the error bars being the sum of excess and bkg, $\sqrt{\text{excess} + \text{bkg}}$. The green band shows the expected emission from the ICS model with a suppressed diffusion coefficient. The SB profiles show good agreement between the data and model. In particular, we see good agreement for the central source and the contamination from its neighboring source in the ROI. In particular, for Geminga, there is a small bump at $\sim$26 pc that is associated with Monogem. Similarly, for Monogem, we see a much larger contamination due to Geminga for distances beyond 30 pc. This is why a simultaneous fit is required for this analysis. The morphology from the surface brightness profiles is compatible with that of HAWC2017.

5.5. Systematics

We studied the systematics associated with the HAWC detector with the procedure described in A. U. Abeysekara et al. (2019). The multisource fit is run with a number of different detector responses generated for the testing of different systematics: angular resolution, analysis bins selection, PMT efficiency/time dependence, PMT threshold, charge uncertainty, and late light simulation. Previous studies in HAWC found no correlation between the systematics (A. U. Abeysekara et al. 2019), allowing a simple addition in quadrature. The systematics introduce an uncertainty to the spectral energy distribution, E^2dN/dE (see Figure 4) in the range of $\sim^{+0.18\%}_{-0.28\%}$ at 1 TeV and $\sim^{+0.16\%}_{-0.1\%}$ at 100 TeV for Geminga; similarly, for Monogem, there is an additional uncertainty in the range of $\sim^{+0.1\%}_{-0.22\%}$ at 1 TeV and $\sim^{+0.14\%}_{-0.12\%}$ at 100 TeV. This is the green band in Figure 4. We list the systematic uncertainties in Table 1.

5.6. Energy-dependent Morphology

We investigate the energy-dependent morphology for Geminga and Monogem in three energy regions: 1–17, 17–31, and 31–316 TeV. We fit the diffusion coefficient at

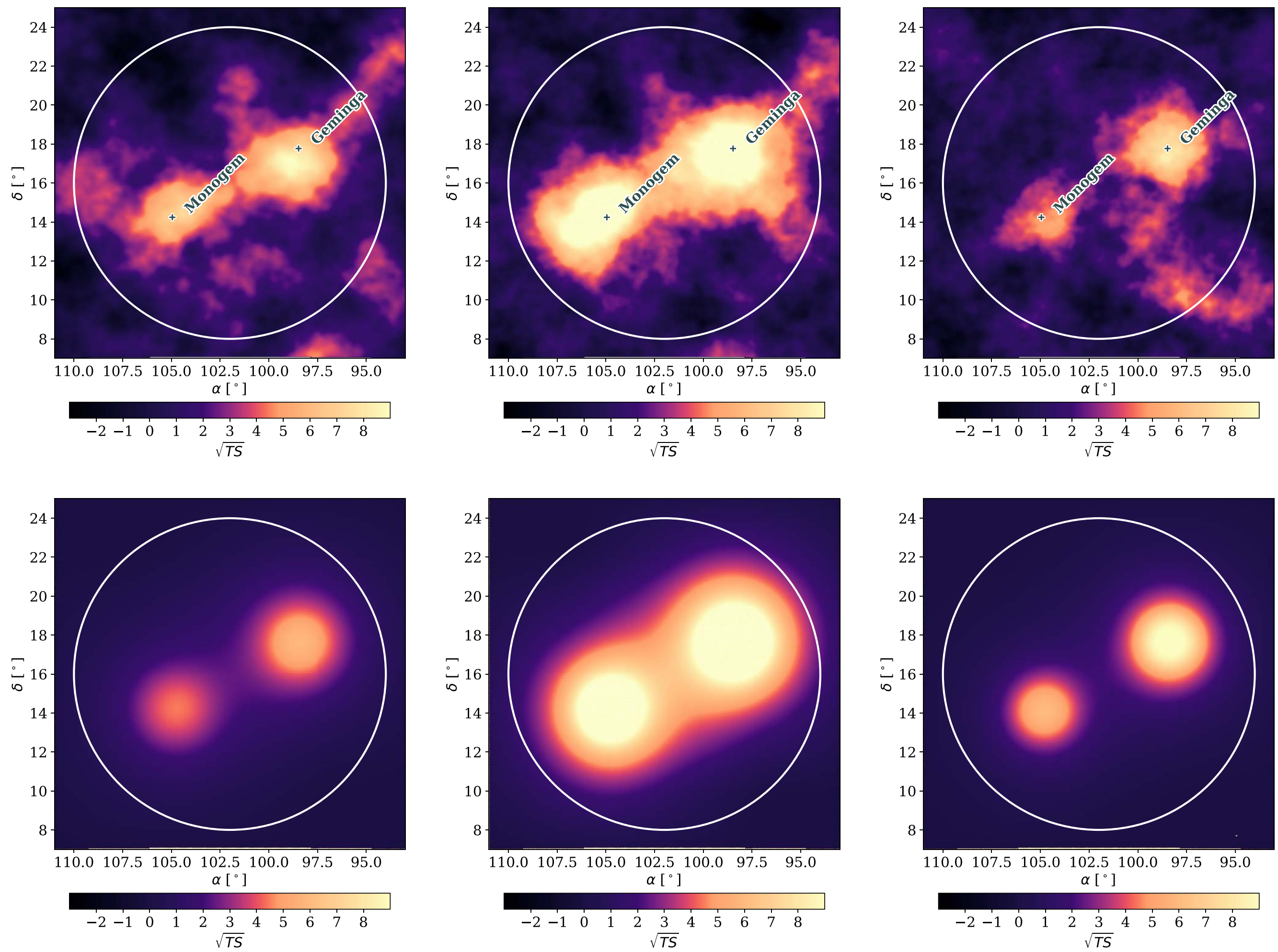

Figure 6. Significance maps of data (top) and model (bottom) for the Geminga region for three energy bands: 1–17 TeV (left), 17–31 TeV (center), and 31–316 TeV (right). The maps are generated with a spatial shape model of 1°.5 disk and the best-fit spectra from Table 1.

Table 5
Best-fit Results for the Diffusion Coefficient of Geminga and Monogem at Three Different Electron Energy Bands: 24, 100, and 160 TeV

Source	$E_e = 24$ TeV			$E_e = 100$ TeV			$E_e = 160$ TeV		
	$D_0 \pm$ stat. $[10^{25}$ cm^2 s$^{-1}]$	$D_{24} \pm$ stat. $[10^{27}$ cm^2 s$^{-1}]$	TS	$D_0 \pm$ stat. $[10^{25}$ cm^2 s$^{-1}]$	$D_{100} \pm$ stat. $[10^{27}$ cm^2 s$^{-1}]$	TS	$D_0 \pm$ stat. $[10^{25}$ cm^2 s$^{-1}]$	$D_{160} \pm$ stat. $[10^{27}$ cm^2 s$^{-1}]$	TS
Geminga	$7.20^{+1.67}_{-1.36}$	$2.00^{+0.46}_{-0.37}$	289	$9.80^{+2.15}_{-1.71}$	$4.40^{+0.66}_{-0.57}$	512	$13.8^{+2.00}_{-1.78}$	$7.60^{+1.44}_{-1.23}$	403
Monogem	$10.20^{+1.79}_{-1.05}$	$2.80^{+0.50}_{-0.42}$	202	$13.2^{+3.04}_{-2.47}$	$5.90^{+1.37}_{-1.11}$	369	$18.20^{+6.92}_{-5.01}$	$9.50^{+3.68}_{-2.67}$	124

Notes. The first diffusion coefficients are at an electron energy of 1 GeV and the latter is the diffusion coefficient evaluated at the electron energies assuming $\delta = 1/3$. The spectral index is fixed to the best-fit result of Table 1.

each of these bands, with the spectral index fixed to the best-fit results from Table 1. The diffusion coefficients are evaluated at the spectrum-weighted median γ-ray energies of 1.8, 20, and 40 TeV that correspond to electron energies 24, 100, and 160 TeV using $\bar{E}_e \approx 17\bar{E}_\gamma^{0.54+0.046\log_{10}(\bar{E}_\gamma/\mathrm{TeV})}$, derived in HAWC2017. The diffusion coefficients at those energies are then scaled to the pivot energy of an electron energy of 1 GeV with

$$D(E_e) = D_0(E_e/1\ \mathrm{GeV})^\delta, \tag{16}$$

where δ is $1/3$, assuming the Kolmogorov model (A. N. Kolmogorov 1941). The best-fit values are reported, including the TS values in Table 5. When comparing the diffusion coefficients at 100 TeV we again find values comparable to the previous estimate of $(4.5 \pm 1.2) \times 10^{27}$ cm^2 s^{-1} from HAWC2017. We can also find that the diffusion coefficient at 160 TeV comparable to the estimate by the LHAASO collaboration for PSR J0622+3749 of $8.9^{+4.5}_{-3.9} \times 10^{27}(d/1.6\ \mathrm{kpc})^2$ cm^2 s^{-1} (F. Aharonian et al. 2021).

We estimated the diffusion index, δ, by a function of the form of Equation (16) over the diffusion coefficients in Table 5 for both sources. We obtain the best-fit values of $\delta = 0.66 \pm 0.13$ for Geminga and $\delta = 0.58 \pm 0.14$ for Monogem. The scaling relation suggests that the energy evolution is

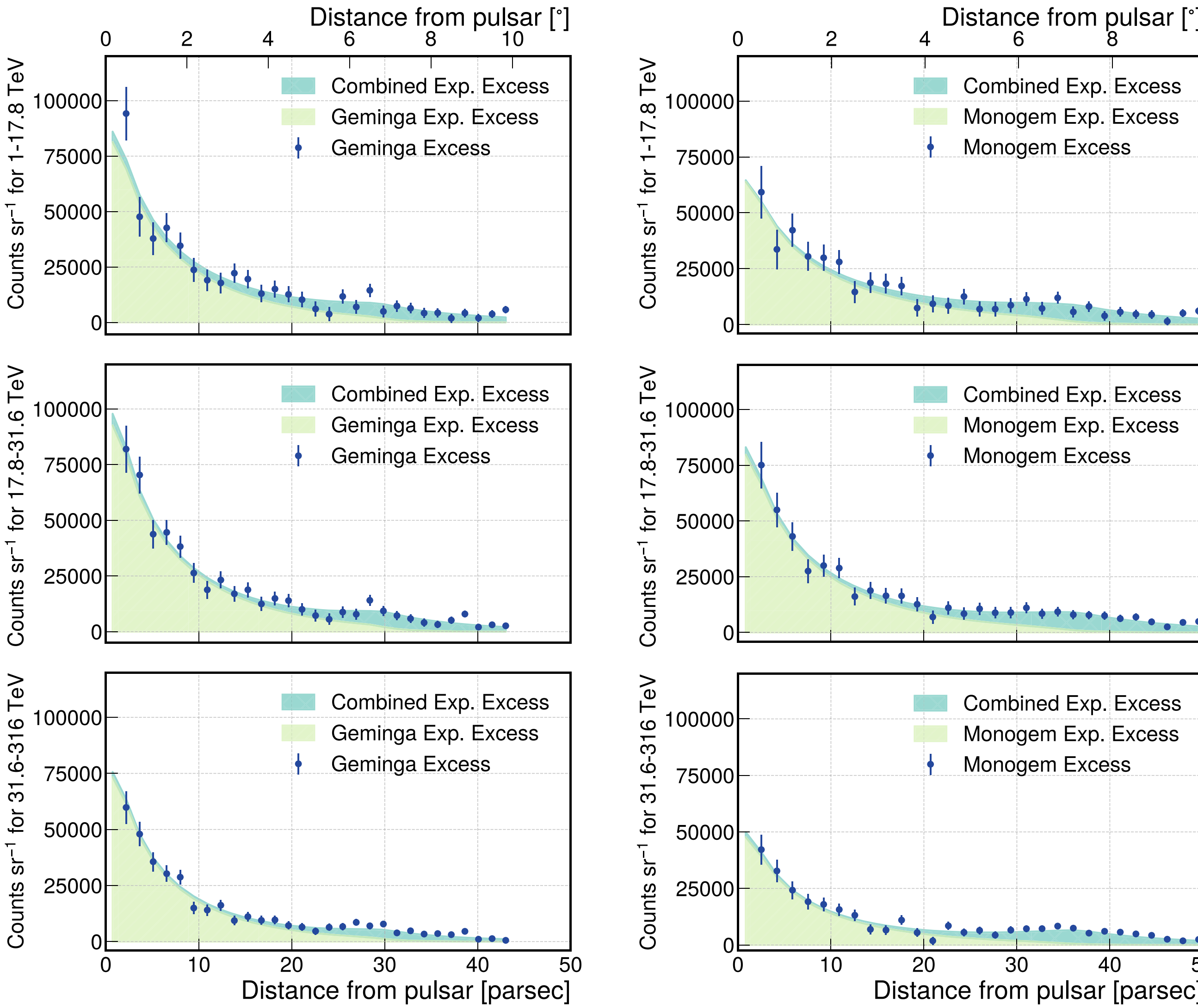

Figure 7. Radial profile of Geminga (left) and Monogem (right) divided into three energy bins. Top: for energies of 1–17 TeV. Middle: for energies of 17–31 TeV. Bottom: for energies of 31–316 TeV. Radial profiles show no significant change for the three different energy bands.

closer to an index of $1/2$, given that our results have a difference of $\sim 2.5\sigma$ and $\sim 2\sigma$, respectively, from the value of $1/3$. However, the uncertainties in our results prevent a clear distinction between indexes of $1/3$ and $1/2$. Therefore, probing the evolution of the diffusion coefficient over a larger energy range would help provide a stronger constraint on the value of δ.

We show the significance maps for the three energy bands in Figure 6. The maps are generated with a 1°.5 disk spatial morphology, but with the best-fit spectrum from Table 1. The upper panel shows the significance map for data, while the bottom panel shows the model maps. The corresponding significances are: 5.9σ, 16σ, and 9.8σ for Geminga, and 4.39σ, 14σ, and 6σ for Monogem. The discrepancy between the TS from the source fit and the significance maps is the morphology of the spatial shape assumed during the multisource fit. The radial profiles for the three energy bands are shown in Figure 7. Similarly to Figure 5, here the green band shows the model contribution from a single source and the blue band shows the contribution from its neighboring source. There is no evident change in morphology in the radial profiles at the three energy bands. For Monogem, we see the contamination from Geminga at distances beyond 30 pc for all energy bands.

5.7. Asymmetry

We investigate the presence of asymmetry by dividing the region around both Geminga and Monogem in four quadrants and fitted the diffusion coefficient. The spectral index is fixed to the best-fit value of Table 1. To reduce the contamination, the emission from the neighboring sources is subtracted. The quadrants are defined as follows:

1. Q1: R.A. $>$ R.A.$_{\rm source}$ and decl. $>$ decl.$_{\rm source}$,
2. Q2: R.A. $<$ R.A.$_{\rm source}$ and decl. $>$ decl.$_{\rm source}$,
3. Q3: R.A. $<$ R.A.$_{\rm source}$ and decl. $<$ decl.$_{\rm source}$, and
4. Q4: R.A. $>$ R.A.$_{\rm source}$ and decl. $<$ decl.$_{\rm source}$.

The results are shown in Table 6. From the best-fit results, we can see that the values differ by $\gtrsim 2\sigma$ in both diffusion coefficient and emission efficiency. More observations are needed to corroborate asymmetric diffusion, as suggested by R. Lopez-Coto & G. Giacinti (2018).

Table 6
Diffusion Coefficient and Emission Efficiency for Four Quadrants around Geminga and Monogem

Quadrant	Best-fit Values	Source	
		Geminga	Monogem
Q1	$D_0 \pm$ stat [10^{25} cm^2 s^{-1}]	$5.40^{+1.70}_{-1.30}$	$11.50^{+3.60}_{-2.70}$
	$\eta \pm$ stat [10^{-2}]	4.50 ± 0.70	5.20 ± 0.70
	TS	152	123
Q2	$D_0 \pm$ stat [10^{25} cm^2 s^{-1}]	$18.20^{+4.10}_{-3.40}$	$6.70^{+1.95}_{-1.51}$
	$\eta \pm$ stat [10^{-2}]	6.10 ± 0.9	4.40 ± 0.6
	TS	249	190
Q3	$D_0 \pm$ stat [10^{25} cm^2 s^{-1}]	$18.60^{+3.70}_{-3.10}$	53.70^{+33}_{-20}
	$\eta \pm$ stat [10^{-2}]	9.70 ± 1.10	7.50 ± 2.20
	TS	450	97
Q4	$D_0 \pm$ stat [10^{25} cm^2 s^{-1}]	$11^{+2.80}_{-2.20}$	$12^{+3.40}_{-2.60}$
	$\eta \pm$ stat [10^{-2}]	7.70 ± 0.80	5.50 ± 0.80
	TS	285	182

Notes. The TS is reported for each of the quadrants. The spectral index is fixed to the best-fit value of Table 1.

6. Discussion

6.1. Other Diffusion Models

Other physical processes, such as ballistic propagation as presented in S. Recchia et al. (2021), have been claimed to be able to fit the surface brightness of these two sources. The authors suggest that $e^{\pm}$ injected by pulsars undergo quasi-ballistic propagation for distances of up to $\lesssim$30 pc at multi-TeV energies. Therefore, when the transition from quasi-ballistic to a diffusive region is considered, HAWC data can be used to fit the morphology of γ-ray halos with diffusion coefficients that are consistent with the average Galactic value. However, the efficiency needed to fit the Geminga surface brightness can be larger than the total spin-down luminosity of the pulsar, as shown in L.-Z. Bao et al. (2022). A conclusive statement about the ballistic interpretation needs to fully account for the magnetic turbulence around the pulsars, which can make the diffusion anisotropic and thus reduce significantly the efficiency needed to fit the data (e.g., R.-Y. Liu et al. 2019).

6.2. Comparison to HAWC2017

We summarize here the differences in methodologies between our current work and HAWC2017. The current work models the diffuse γ-ray emission from pulsar properties (see Section 1). In HAWC2017, the authors utilized an approximated solution to the electron number distribution integrated along the line of sight (see S4 in supplemental materials of HAWC2017). This suggests an overestimate of the diffusion radius and in turn diffusion coefficient. We compare the derived diffusion coefficients and electron/positron emission efficiencies under the assumption that the diffusion coefficient changes with energy with Equation (16) using the diffusion coefficient from Table 1, and δ is assumed to be $1/3$ as it was done in HAWC2017. The derived coefficients at an energy of 100 TeV (referred to as D_{100}) from this work are respectively $D_{100} = (4.78^{+0.94}_{-0.80}) \times 10^{27}$ cm^2 s^{-1} and $D_{100} = (6.57^{+0.62}_{-1.08}) \times 10^{27}$ cm^2 s^{-1}. Our estimates are consistent within $\sim 1\sigma$ from the previous result, $(4.5 \pm 1.2) \times 10^{27}$ cm^2 s^{-1}, assumed for both sources. After conducting a joint fit for the diffusion coefficient, we estimate a diffusion coefficient of $(1.5 \pm 0.11) \times 10^{26}$ cm^2 s^{-1} at 1 GeV, or $D_{100} = 6.76^{+0.51}_{-0.48} \times 10^{27}$ cm^2 s^{-1}, which is again comparable to the result from HAWC2017. In HAWC2017, they assumed an ISRF model described by three blackbody distributions (see Table 1 in supplemental materials of HAWC2017). We use the ISRF model from S. Vernetto & P. Lipari (2016) with no approximation. The blackbody approximation results in an ISRF spectrum with an emission that is 25% lower than the complete model for frequencies in the range of 10^{13}–10^{14} Hz. This suggests higher emission efficiencies under the blackbody emission model. Therefore, using the blackbody approximation, higher efficiencies are found. This can account for the discrepancy in our best estimate $\sim$6.1% for Geminga and 5.1% for Monogem, which differs significantly from the values reported in HAWC2017 of 40% and 4%, respectively.

The authors of G. Johannesson et al. (2019) find that the spectrum shape of $e^{\pm}$ and energy range of injection play a major effect on the emission efficiency. For spectra with softer values, α_e yields fewer $e^{\pm}$ at TeV energies, so higher efficiencies are required to coincide with HAWC observations (M. Di Mauro et al. 2019). We find spectral indices of $0.95^{+0.08}_{-0.09}$ for Geminga and $1.06^{+0.09}_{-0.10}$ for Monogem, which helps support our estimates of lower emission efficiencies.

6.3. Comparison with Fermi-LAT

In M. Di Mauro et al. (2019), the authors analyzed the extended γ-ray halos around Geminga and Monogem with 115 months of *Pass8* data from Fermi-LAT. They considered an energy range between 8 GeV and 1 TeV and assumed a considerably larger ROI of $70° \times 70°$. This choice is motivated by the fact that, at GeV energies, below the HAWC energy range, the $e^{\pm}$ cooling time is on the scale of the pulsar age and therefore requires a larger extent. They report a diffusion coefficient in the range of $1.6-3.5 \times 10^{26}$ cm^2 s^{-1} at 1 GeV, assuming the interstellar emission models used in F. Acero et al. (2016) and M. Ackermann et al. (2017). They provide a weighted average of 2.3×10^{26} cm^2 s^{-1} at 1 GeV. Our best-fit value for Geminga 1.07×10^{26} cm^2 s^{-1} is $\sim 1/2$ from their estimate. They fitted the HAWC data assuming three spectral indices $\alpha_e = [1.8, 1.9, 2.0]$ and obtained emission efficiencies of $\eta = [0.24, 0.16, 0.13]$ for Geminga. For Monogem, they used $\alpha_e = [1.9, 2.1]$ and derived an upper limit of $\eta \leqslant 0.011$ and 0.009, respectively. In comparison, our best-fit to HAWC data suggests an emission efficiency of Geminga $\sim$3 times smaller than their estimate. Furthermore, the emission efficiency for Monogem is $\sim$5 times higher than their upper limit. In any case, these numbers should be taken with some care because the injection spectrum we use has a different shape than the one in M. Di Mauro et al. (2019).

6.4. Comparison with H.E.S.S

The H.E.S.S collaboration studied the extended emission of Geminga with observations from 2006 to 2008 with a total of 14.2 hr and an additional data set obtained during the first quarter of 2019 with total live time of 27.2 hr. They estimate a diffusion coefficient for Geminga of $D(E_e) = (7.5^{+1.6}_{-1.2}) \times 10^{27}$ cm^2 s^{-1} at an electron energy of 100 TeV with two different background estimation methods, on-and-off and ring for a radius of 1° around Geminga, and estimate the emission to extend up to $\sim$3° for energies of 5–40 TeV (H.E.S.S. Collaboration et al 2023). Our estimate agrees with that of H.E.S.S. for the diffusion coefficient for the individual and combined fit of Geminga. It is worth mentioning that full γ-ray emission of Geminga is beyond the available sky region, i.e., their current observation data set. Therefore, their size estimate should be treated as a lower limit (H.E.S.S. Collaboration et al 2023).

6.5. Physical Interpretation

The extended γ-ray emission around Geminga and Monogem is consistent with electrons and positrons being accelerated by the PWNe and injected in the interstellar medium. The injection spectrum can be modeled with a power law with a quite hard slope of around 1 with a cutoff above tens of TeV. The slope could achieve softer values by reducing the cutoff energy. Moreover, the efficiency required to fit the data is about 5%−6%, which is of the same order of the one needed to explain previous HAWC data and the detection of the Geminga halo at GeV energies in Fermi-LAT data M. Di Mauro et al. (2019). We also confirm, with good precision, that the size of extension of the detected halos around Geminga and Monogem can be fitted only if we assume a diffusion coefficient around these two pulsars that is about a factor of 100 smaller than the average value assumed in the Galactic halo to fit primary and secondary cosmic rays (see, e.g., M. Di Mauro et al. 2023a, 2023b). The inhibited diffusion should be extended at least 30–40 pc. The physical interpretation on the contribution from Geminga to the positron flux can vary due to the choice of the spatial extension of the inhibited diffusion around the pulsar. Local pulsars, such as Geminga, can produce a sizeable part of the positron flux measured by AMS-02 above 10 GeV (M. Aguilar et al. 2019). In fact, as already discussed, for example, in M. Di Mauro et al. (2019a) and L. Orusa et al. (2021), Geminga alone can produce about a few tens of percent of the total measured flux, assuming a two-zone diffusion model. On the other hand, when assuming that the diffusion coefficient is inhibited in the entire Galactic disk, as in HAWC2017, the contribution of Geminga can be negligible.

7. Conclusions

In this paper, we presented a follow-up analysis of the physical interpretation of the γ-ray halos surrounding the Geminga and Monogem pulsars. We employed a template fitting method that allows for the direct modeling of spatial and spectral morphology of $e^{\pm}$ ICS diffuse γ-ray emission from interactions with the interstellar medium (ISM).

We further constrain the diffusion coefficients for regions around Geminga and Monogem 4.78 to 7×10^{27} cm^2 s^{-1} at an electron energy of 100 TeV. This confirms the presence of an inhibited diffusion region, which differs by a factor of 100 from the average Galactic value that extends up to 30 to 40 pc from the pulsars. The above conclusion is further verified by the agreement between data and model using surface brightness profiles.

Current experiments such as HAWC, LHAASO, and the future SWGO are expected to increase the number of TeV halo candidates. These observations are essential to perform a pulsar halo population study to determine whether diffusion inhibited regions are an innate characteristic or a product of their environment. Moreover, observations from Imaging Air Cherenkov telescopes (IACTs) such as VERITAS, MAGIC, and HESS, as well as the future CTA, are also essential for the morphology study of pulsar halos at angular scales that are unachievable for wide field-of-view γ-ray observatories.

Acknowledgments

We acknowledge the support from: the US National Science Foundation (NSF); the US Department of Energy Office of High-Energy Physics; the Laboratory Directed Research and Development (LDRD) program of Los Alamos National Laboratory; Consejo Nacional de Ciencia y Tecnología (CONACyT), México, grants LNC-2023-117, 271051, 232656, 260378, 179588, 254964, 258865, 243290, 132197, A1-S-46288, A1-S-22784, CF-2023-I-645, cátedras 873, 1563, 341, 323, Red HAWC, México; DGAPA-UNAM grants IG101323, IN111716-3, IN111419, IA102019, IN106521, IN114924, IN110521, IN102223; VIEP-BUAP; PIFI 2012, 2013, PROFOCIE 2014, 2015; the University of Wisconsin Alumni Research Foundation; the Institute of Geophysics, Planetary Physics, and Signatures at Los Alamos National Laboratory; Polish Science Centre grant, DEC-2017/27/B/ST9/02272; Coordinación de la Investigación Científica de la Universidad Michoacana; Royal Society - Newton Advanced Fellowship 180385; Generalitat Valenciana, grant CIDEGENT/2018/034; The Program Management Unit for Human Resources & Institutional Development, Research and Innovation, NXPO (grant number B16F630069); Coordinación General Académica e Innovación (CGAI-UdeG), PRODEP-SEP UDG-CA-499; Institute of Cosmic Ray Research (ICRR), University of Tokyo; National Research Foundation of Korea (RS-2023-00280210). We also acknowledge the significant contributions over many years of Stefan Westerhoff, Gaurang Yodh and Arnulfo Zepeda Domínguez, all deceased members of the HAWC collaboration. Thanks to Scott Delay, Luciano Díaz and Eduardo Murrieta for technical support. R.T.E. would like to acknowledge the support of University of Delaware and the Fermi Summer School and the number of experts that make the introduction to the field of astroparticle physics easier. R.T.E. would like to thank Dr. Nural Akchurin for the support and guidance through graduate school at Texas Tech University. E.d.l.F. thanks cuerpo academico UDG-CA-499 and several PRO-SNI local projects that support this work. H.Z. and R.T.E. also would like to acknowledge the support of grant No. 12393853 from the National Science Foundation of China (NSFC).

M.D.M. acknowledges support from the Research grant TAsP (Theoretical Astroparticle Physics) funded by Istituto Nazionale di Fisica Nucleare (INFN).

Facility: HAWC.

Software: Figure formatting (A. Novak et al. 2020).

ORCID iDs

A. Albert https://orcid.org/0000-0003-0197-5646
D. Avila Rojas https://orcid.org/0000-0002-4020-4142
H. A. Ayala Solares https://orcid.org/0000-0002-2084-5049
R. Babu https://orcid.org/0000-0002-5529-6780
E. Belmont-Moreno https://orcid.org/0000-0003-3207-105X
K. S. Caballero-Mora https://orcid.org/0000-0002-4042-3855
A. Carramiñana https://orcid.org/0000-0002-8553-3302
S. Casanova https://orcid.org/0000-0002-6144-9122
U. Cotti https://orcid.org/0000-0002-7607-9582
J. Cotzomi https://orcid.org/0000-0002-1132-871X
S. Coutiño de León https://orcid.org/0000-0002-7747-754X
E. de la Fuente https://orcid.org/0000-0001-9643-4134

D. Depaoli https://orcid.org/0000-0002-2672-4141
N. Di Lalla https://orcid.org/0000-0002-7574-1298
B. L. Dingus https://orcid.org/0000-0001-8451-7450
M. A. DuVernois https://orcid.org/0000-0002-2987-9691
M. Durocher https://orcid.org/0000-0003-2169-0306
J. C. Díaz-Vélez https://orcid.org/0000-0002-0087-0693
K. Engel https://orcid.org/0000-0001-5737-1820
C. Espinoza https://orcid.org/0000-0001-7074-1726
K. L. Fan https://orcid.org/0000-0002-8246-4751
N. Fraija https://orcid.org/0000-0002-0173-6453
J. A. García-González https://orcid.org/0000-0002-4188-5584
M. M. González https://orcid.org/0000-0002-5209-5641
J. A. Goodman https://orcid.org/0000-0002-9790-1299
J. P. Harding https://orcid.org/0000-0001-9844-2648
I. Herzog https://orcid.org/0000-0001-5169-723X
P. Hüntemeyer https://orcid.org/0000-0002-3302-7897
D. Huang https://orcid.org/0000-0002-5447-1786
F. Hueyotl-Zahuantitla https://orcid.org/0000-0002-5527-7141
D. Kieda https://orcid.org/0000-0003-4785-0101
A. Lara https://orcid.org/0000-0001-6336-5291
W. H. Lee https://orcid.org/0000-0002-2467-5673
H. León Vargas https://orcid.org/0000-0001-5516-4975
J. T. Linnemann https://orcid.org/0000-0003-2696-947X
A. L. Longinotti https://orcid.org/0000-0001-8825-3624
G. Luis-Raya https://orcid.org/0000-0003-2810-4867
K. Malone https://orcid.org/0000-0001-8088-400X
O. Martinez https://orcid.org/0000-0001-9052-856X
J. Martínez-Castro https://orcid.org/0000-0002-2824-3544
J. A. Matthews https://orcid.org/0000-0002-2610-863X
P. Miranda-Romagnoli https://orcid.org/0000-0002-8390-9011
E. Moreno https://orcid.org/0000-0002-1114-2640
M. Mostafá https://orcid.org/0000-0002-7675-4656
A. Nayerhoda https://orcid.org/0000-0003-0587-4324
L. Nellen https://orcid.org/0000-0003-1059-8731
R. Noriega-Papaqui https://orcid.org/0000-0001-7099-108X
L. Olivera-Nieto https://orcid.org/0000-0002-9105-0518
N. Omodei https://orcid.org/0000-0002-5448-7577
Y. Pérez Araujo https://orcid.org/0000-0002-8774-8147
E. G. Pérez-Pérez https://orcid.org/0000-0001-5998-4938
C. D. Rho https://orcid.org/0000-0002-6524-9769
D. Rosa-González https://orcid.org/0000-0003-1327-0838
A. Sandoval https://orcid.org/0000-0001-6079-2722
M. Schneider https://orcid.org/0000-0001-8644-4734
R. W. Springer https://orcid.org/0000-0002-1492-0380
K. Tollefson https://orcid.org/0000-0001-9725-1479
I. Torres https://orcid.org/0000-0002-1689-3945
R. Torres-Escobedo https://orcid.org/0000-0002-0786-7307
R. Turner https://orcid.org/0000-0003-1068-6707
F. Urea-Mena https://orcid.org/0000-0002-2748-2527
E. Varela https://orcid.org/0000-0003-0715-7513
L. Villaseñor https://orcid.org/0000-0001-6876-2800
X. Wang https://orcid.org/0000-0001-6798-353X
I. J. Watson https://orcid.org/0000-0003-2141-3413
E. Willox https://orcid.org/0000-0002-6623-0277
H. Wu https://orcid.org/0009-0005-7243-1402
S. Yun-Cárcamo https://orcid.org/0000-0002-9307-0133
H. Zhou https://orcid.org/0000-0003-0513-3841
M. Di Mauro https://orcid.org/0000-0003-2759-5625

References

Abdo, A. A., Allen, B., Berley, D., et al. 2007, ApJ, 664, L91
Abeysekara, A. U., Albert, A., Alfaro, R., et al. 2017a, Sci, 358, 911
Abeysekara, A. U., Albert, A., Alfaro, R., et al. 2017b, ApJ, 843, 40
Abeysekara, A. U., Albert, A., Alfaro, R., et al. 2017c, ApJ, 843, 39
Abeysekara, A. U., Albert, A., Alfaro, R., et al. 2019, ApJ, 881, 134
Abeysekara, A. U., Albert, A., Alfaro, R., et al. 2021, ICRC (Berlin), 37, 828
Abeysekara, A. U., Albert, A., Alfaro, R., et al. 2023, NIMPA, 1052, 168253
Acero, F., Ackermann, M., Ajello, M., et al. 2016, ApJS, 224, 8
Ackermann, M., Ajello, M., Allafort, A., et al. 2012, PhRvL, 108, 011103
Ackermann, M., Ajello, M., Albert, A., et al. 2017, ApJ, 840, 43
Adriani, O., Barbarino, G. C., Bazilevskaya, G. A., et al. 2013, PhRvL, 111, 081102
Aguilar, M., Ali Cavasonza, L., Ambrosi, G., et al. 2021, PhR, 894, 1
Aguilar, M., Ali Cavasonza, L., Ambrosi, G., et al. 2019, PhRvL, 122, 041102
Aharonian, F., An, Q., & Axikegu, L. X. 2021, B., et al, PhRvL, 126, 241103
Aharonian, F. A., Atoyan, A. M., & Voelk, H. J. 1995, A&A, 294, L41
Albert, A., Alfaro, R., Alvarez, C., et al. 2020, ApJ, 905, 76
Albert, A., Alfaro, R., Arteaga-Velazquez, J. C., et al. 2023, ApJL, 944, L29
Albert, A., Alfaro, R., Alvarez, C., et al. 2024, arXiv:2405.06050
Atoyan, A. M., Aharonian, F. A., & Volk, H. J. 1995, PhRvD, 52, 3265
Bao, L.-Z., Fang, K., Bi, X.-J., & Wang, S.-H. 2022, ApJ, 936, 183
Berezinskiĭ, V. S., Bulanov, V. S., Dogiel, V. A., & Ginzburg, V. 1990, Astrophysics of Cosmic Rays (Amsterdam: North Holland)
Cholis, I., Karwal, T., & Kamionkowski, M. 2018, PhRvD, 98, 063008
Delahaye, T., Lineros, R., Donato, F., et al. 2009, A&A, 501, 821
Di Mauro, M., Donato, F., Fornengo, N., Lineros, R., & Vittino, A. 2014, JCAP, 04, 006
Di Mauro, M., Donato, F., Korsmeier, M., Manconi, S., & Orusa, L. 2023a, PhRvD, 108, 063024
Di Mauro, M., Korsmeier, M., & Cuoco, A. 2023b, arXiv:2311.17150
Di Mauro, M., Manconi, S., & Donato, F. 2019, PhRvD, 100, 123015
Di Mauro, M., Manconi, S., & Donato, F. 2020, PhRvD, 101, 103035
Di Mauro, M., Manconi, S., Negro, M., & Donato, F. 2021, PhRvD, 104, 103002
Evoli, C., Linden, T., & Morlino, G. 2018, PhRvD, 98, 063017
Giacinti, G., Mitchell, A. M. W., López-Coto, R., et al. 2020, A&A, 636, A113
Harding, A. K., & Ramaty, R. 1987, ICRC (Moscow), 20, 92
H.E.S.S. Collaboration, Aharonian, F., Ait Benkhali, F., et al. 2023, A&A., 673, A148
Hooper, D., Blasi, P., & Serpico, P. D. 2009, JCAP, 2009, 025
Hooper, D., Cholis, I., Linden, T., & Fang, K. 2017, PhRvD, 96, 103013
Hooper, D., & Linden, T. 2022, PhRvD, 105, 103013
Johannesson, G., Porter, T. A., & Moskalenko, I. V. 2019, ApJ, 879, 91
Kass, R. E., & Raftery, A. E. 1995, J. Am. Stat. Assoc., 90, 773
Kolmogorov, A. N. 1941, DoSSR, 30, 301
Korsmeier, M., & Cuoco, A. 2022, PhRvD, 105, 103033
Liddle, A. R. 2007, MNRAS: Lett., 377, L74
Lingenfelter, R. E. 1973, Ap&SS, 24, 83
Liu, R.-Y. 2022, IJMPA, 37, 2230011
Liu, R.-Y., Yan, H., & Zhang, H. 2019, PhRvL, 123, 221103
Lopez-Coto, R., de Ona Wilhelmi, E., Aharonian, F., Amato, E., & Hinton, J. 2022, NatAs, 6, 199
Lopez-Coto, R., & Giacinti, G. 2018, MNRAS, 479, 4526
Manchester, R. N., Hobbs, G. B., Teoh, A., & Hobbs, M. 2005, AJ, 129, 1993
Moskalenko, I. V., & Strong, A. W. 1998, ApJ, 493, 694
Mukhopadhyay, P., & Linden, T. 2022, PhRvD, 105, 123008
Novak, A., Schreiner, H., & Feickert, M., 2020 mplhep, Zenodo, doi:10.5281/ZENODO.3766157
Orusa, L., Manconi, S., Donato, F., & Di Mauro, M. 2021, JCAP, 12, 014
Ostriker, J. P., & Gunn, J. E. 1969, ApJ, 157, 1395
Popescu, C. C., Yang, R., Tuffs, R. J., et al. 2017, MNRAS, 470, 2539
Posselt, B., Pavlov, G. G., Slane, P. O., et al. 2017, ApJ, 835, 66
Recchia, S., Di Mauro, M., Aharonian, F. A., et al. 2021, PhRvD, 104, 123017
Schroer, B., Evoli, C., & Blasi, P. 2023, PhRvD, 107, 123020
Smith, A. J. 2016, ICRC (The Hague), 34, 966
Sudoh, T., Linden, T., & Beacom, J. F. 2019, PhRvD, 100, 043016
Trotta, R., Johannesson, G., Moskalenko, I. V., et al. 2011, ApJ, 729, 106
Vernetto, S., & Lipari, P. 2016, PhRvD, 94, 063009
Vianello, G., Lauer, R. J., Younk, P., et al. 2015, arXiv:1507.08343
Wilks, S. S. 1938, Ann. Math. Stat., 9, 60
Yuksel, H., Kistler, M. D., & Stanev, T. 2009, PhRvL, 103, 051101